Densification of Ionic Liquid Electrospray Thrusters using Silicon-Based MEMS Fabrication

Densification of Ionic Liquid Electrospray Thrusters using Silicon-Based MEMS Fabrication

IEPC-2022-177

Presented at the 37th International Electric Propulsion Conference
Massachusetts Institute of Technology, Cambridge, MA, USA
June 19-23, 2022

Matthew N. Corrado[1] and Paulo C. Lozano[2]
Massachusetts Institute of Technology, Cambridge, MA, USA

Lalitha Parameswaran[3], Matthew Cook[4], Eric C. Holihan[5], Richard Mathews[6], Livia M. Racz[7], and Melissa A. Smith[8]
MIT Lincoln Laboratory, Lexington, MA, USA

Ionic liquid electrospray propulsion is an attractive alternative to both chemical space propulsion and traditional electric space propulsion due to its unique ability to be scaled down to extremely small sizes and operated using very low power. While electrosprays are one of the most mass- and volume-efficient forms of electric propulsion, their relatively low thrust density prevents their widespread utilization on small satellites limited in external area. To address the deficiency in thrust density, a high-density electrospray thruster, which packs more ion emitter tips per area compared to the current state of the art in electrospray propulsion, is designed and characterized. Silicon-based microelectromechanical systems (MEMS) fabrication techniques are leveraged to create ultra-dense arrays of emitters while maintaining extraordinary precision and resolution in the complex 3D microstructres that form the emitter tips. Thrusters with pitch as low as 127 µm are tested in the Space Propulsion Laboratory at MIT, yielding the first performance estimates for this densified electrospray design and paving a path toward testing and characterization of even further densified 64 µm thrusters. The initial performance is promising, with the thrusters exhibiting stable emission in the pure ionic regime and beam currents exceeding 70 µA at emitter potentials on the order of 1 kV. A direct thrust measurement is taken using a magnetically levitated thrust stand, proving that the thrusters are capable of producing usable and measurable thrust.

I. Introduction

Increased commercial interest in space has motivated the conceptualization and development of enormous constellations of small yet capable satellites. With maneuverability being paramount to the successful deployment and operation of such constellations, miniaturization of in-space propulsion systems, especially high-performance electric propulsion systems, is of key interest. Benefitting from the absence of an ionization volume and scalability down to arbitrarily small sizes, electrospray thrusters are a mass- and volume-efficient propulsion option for small satellites.

Drawbacks to existing instances of electrospray thrusters, primarily their comparatively low thrust density, are addressed through the development of a densified ion electrospray thruster. Densification of arrays of electrospray emitters is achieved using advanced microelectromechanical systems (MEMS) manufacturing techniques, which enable

[1]PhD Candidate, Department of Aeronautics and Astronautics, mcorrado@mit.edu.
[2]M. Alemán-Velasco Professor, Department of Aeronautics and Astronautics, plozano@mit.edu.
[3]Technical Staff, Advanced Technology, lalithap@ll.mit.edu.
[4]Associate Technical Staff, Advanced Technology, matthew.cook@ll.mit.edu.
[5]Associate Technical Staff, Advanced Technology, eric.holihan@ll.mit.edu.
[6]Technical Staff, Advanced Technology, mathews@ll.mit.edu.
[7]Group Leader, Advanced Technology, livia.racz@ll.mit.edu.
[8]Assistant Group Leader, Advanced Technology, melissa.smith@ll.mit.edu.

This material is based upon work supported by the Under Secretary of Defense for Research and Engineering under Air Force Contract No. FA8702-15-D-0001. Any opinions, findings, conclusions or recommendations expressed in this material are those of the author(s) and do not necessarily reflect the views of the Under Secretary of Defense for Research and Engineering.

the fabrication of larger quantities of microscopic ion emitters in significantly smaller footprints, thus increasing the thrust density, or the force produced per unit area of thruster face. Extensive testing and characterization are required to validate the performance and effectiveness of this novel space thruster.

To increase the thrust density of electrospray thrusters, it is necessary to either increase the amount of current extracted per individual emitter tip or increase the number of emitter tips per unit area. The physics of electrospray ion emitters in the pure ion regime (PIR) limit the amount of current capable of being extracted from a single emitter [1, 2]. And, up to this point, difficulty in reliably manufacturing large arrays of emitter tips has limited the minimum achievable tip spacing, or pitch distance, which controls the number of tips per area.

Leveraging advances in silicon-based MEMS fabrication techniques now commonly used in the electronics industry, it is possible to manufacture large arrays of geometrically precise ion emitters with record-breaking densities. Typical pitch distances for state-of-the-art glass-based electrospray thrusters are on the order of 500 microns [3, 4]. Using silicon MEMS techniques, arrays with pitch distances as small as 127 and 64 microns have been fabricated and tested, representing increases in the number of individual emitters in an equal footprint by factors of 15 and 60.

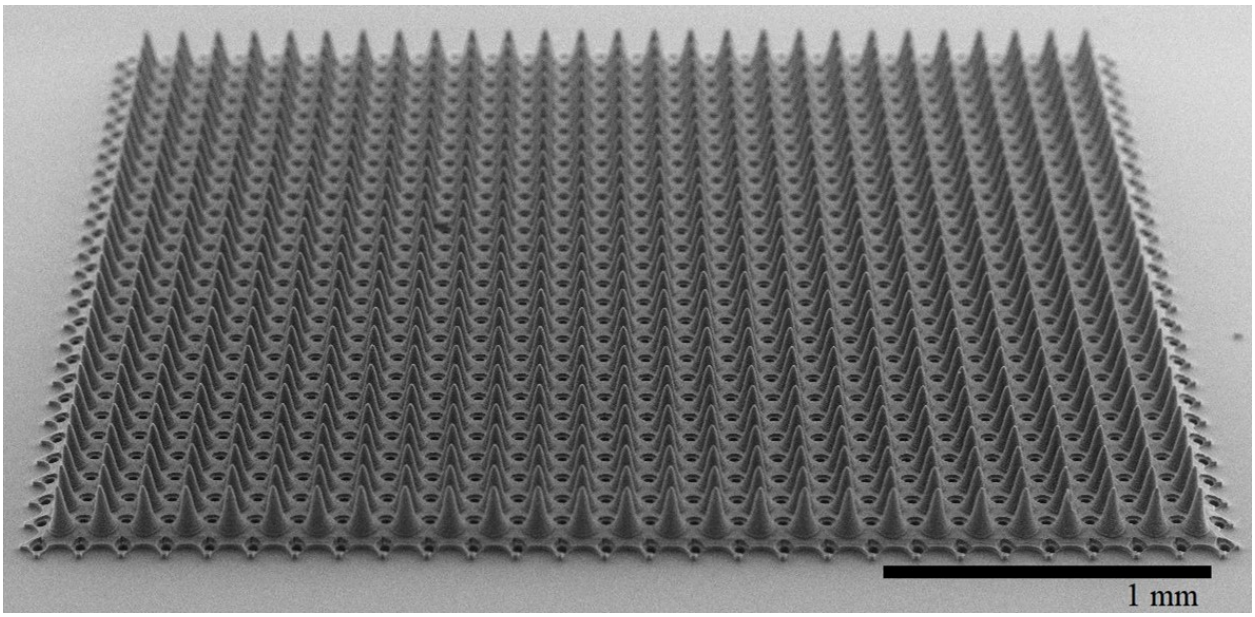

Fig. 1 SEM image of a 729-tip emitter array with a pitch of 127 microns.

The densified electrospray thrusters fabricated from silicon are extensively tested, including both electrical and performance characterization techniques, to highlight the usefulness of the design for missions requiring larger thrust densities. Results from the characterization effort are reported, including tests using diagnostic techniques such as current-voltage response (IV), time-of-flight mass spectrometry (TOF), retarding potential analysis (RPA), and beam divergence measurements. The combination of these results yields estimates for many key performance metrics of the system which would be of interest to space system architects, including thrust density, specific impulse, and efficiency. This work focuses on 127-μm-pitch thrusters, which is the largest density integrated thruster tested and characterized to date. However, the same fabrication techniques are capable of producing 64-μm-pitch devices, and in the future even denser arrays can be fabricated. While 64 μm emitters have been tested independently against a solid electrode, they have not been integrated with semi-transparent extractors to allow for ion expulsion and useful thrust [5]. This work serves as a proof of concept for densified silicon-based electrosprays, and therefore further scaling to even denser and more capable devices is both possible and imminent.

II. Design and Fabrication

The state of the art in electrospray propulsion uses porous glass emitters patterned using laser ablation. While these same fabrication techniques can in principle be used to create thrusters with more densely packed emitter arrays, natural limitations exist to the precision and resolution of laser ablation, so emitter densities approaching the theoretical limit for electrospray propulsion are likely unfeasible. However, extraordinary advances in semiconductor photolithography

fabrication techniques have enabled fabrication of incredibly complex planar structures with feature sizes approaching single nanometers. In three dimensions, techniques such as grayscale lithography can spatially modulate the exposure of a photoresist mask in order to create complex three-dimensional microstructures with smooth facets and resolution better than a single micron [6].

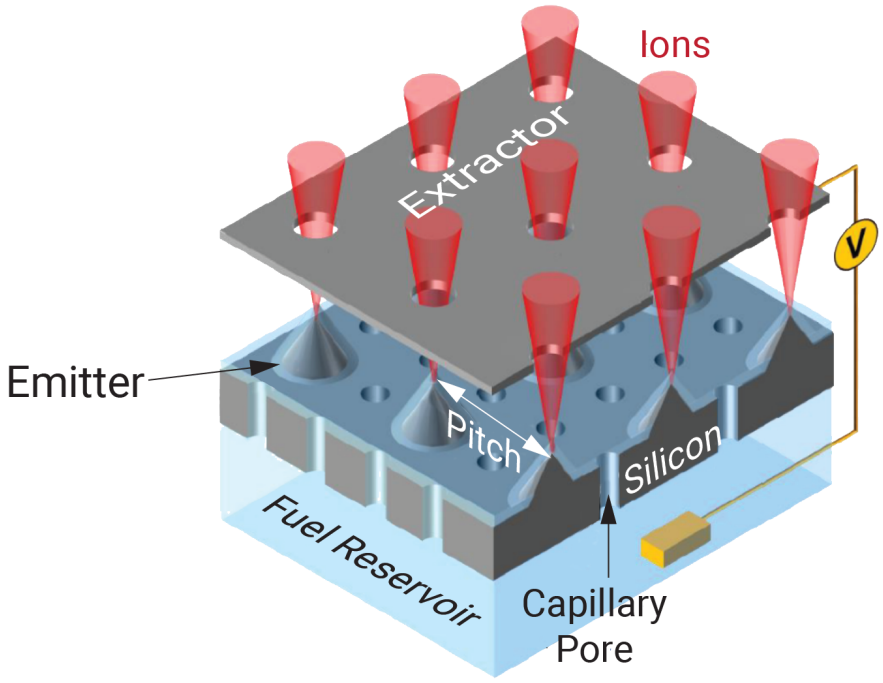

Fig. 2 The tip-capillary architecture of the ultra-dense silicon-based thrusters, diagrammed to highlight the various components and interfaces.

Details regarding the design and development of the densified silicon emitters tested here are included in [5]. The combined tip-capillary architecture illustrated in Fig. 2 allows transport of propellant from an external reservoir to an emission site via a fluid circuit comprised of a thin capillary tube and a porous surface layer. A critical design aspect of electrospray emitters utilizing passive propellant transport is their hydraulic impedance, which is the sole determiner of propellant flow rate. Previous investigations into the properties of the emitters and capillaries that govern hydraulic impedance culminated in a design featuring specific geometries and surface treatments to provide a fluid circuit with impedance compatible with electrosprays in the PIR.

III. Characterization of Integrated Silicon Thrusters

The work of Siegel [5] culminated in test firing of the silicon emitters onto a solid plate electrode. Since the solid electrode was without apertures, it could be shown that the emitters were capable of emitting current, but no thrust was produced as the ions impinged directly onto the plate instead of leaving the system as exhaust. To produce thrust, a semi-transparent extractor must be used to apply the potential difference so that emitted ions can accelerate through the extractor apertures and be expelled from the thruster. An extractor grid was designed to be fabricated from silicon so that they can be efficiently mass-produced using the same silicon MEMS fabrication technology used to fabricate the emitters.

A. Overview of Facilities

The thrusters are tested primarily in the Turbovac vacuum chamber in the Space Propulsion Laboratory (SPL) at MIT. Turbovac is equipped with a mechanical roughing pump and two turbomolecular pumps. Thrusters are tested at pressures $< 5 \times 10^{-6}$ Torr. The chamber is outfitted with various diagnostic instruments, and during testing thrusters are mounted on a rotational stage such that the beam can be aimed at different instruments without breaking vacuum.

High voltage is supplied to the thruster using a Matsusada AP-3B1 high voltage amplifier, and currents through the power supply and through the extractor electrode are measured independently using Analog Devices AD210AN isolation amplifiers. All signals, including voltages, currents, and miscellaneous measurements are collected using a National Instruments USB-6229 DAQ and logged using custom software.

In addition to being able to collect current-voltage (IV) data, the Turbovac chamber is outfitted with a retarding potential analyzer (RPA), a time of flight mass spectrometer (TOF), and a Faraday cup. Each instrument is positioned at a different angle relative to the chamber centerline so that the thruster can be rotated to face any one of them at a time. The details of each of these instruments and the information about thruster performance that they reveal are listed in the following sections.

1. Current-Voltage Characteristic

The current-voltage response of the thruster is characterized by measurement of the ion beam current emitted by the thruster in response to an applied voltage. The results of such experiments indicate the startup voltage of the thruster and is used, in conjunction with other measurements, to evaluate the thrust-to-power ratio achievable by the thruster at different operating points. In addition, a thruster IV curve reveals its ability to be throttled by modulation of the voltage to control the emitted current, which is crucial information for the design of the power electronics that will be used to operate the thrusters.

2. Retarding Potential Analysis

Retarding potential analysis utilizes semi-transparent grids, which can be biased to variable potentials, to determine the energy of the charged particles that exist in the beam. Behind the biased grids sits a Faraday cup for current collection, so the magnitude of current collected behind the grids varies with the potential of the grids. Ions with insufficient energy to overcome the potential field are retarded, while ions with sufficient energy are collected. By performing sweeps on the grid potential, an energy spectrum of the beam particles is obtained, yielding estimates for the efficiency of the ion acceleration process.

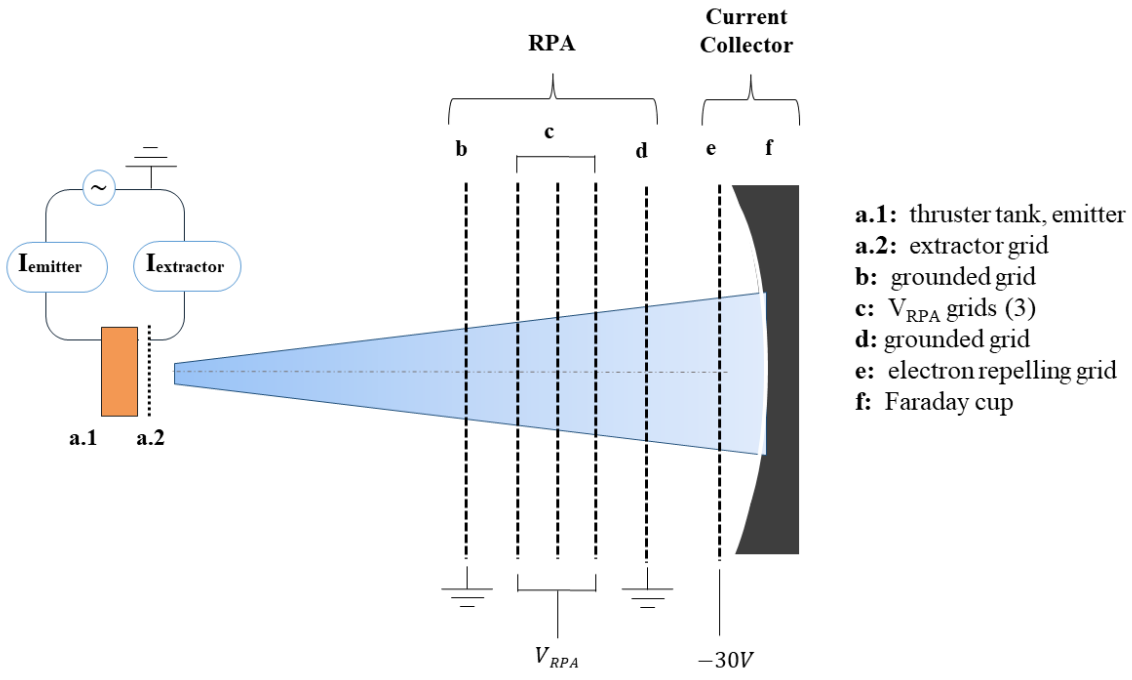

Fig. 3 Diagram of the RPA used in the electrospray tests in the SPL

Fig. 3 shows a diagram of the RPA used in these tests. Several grids are placed in series, including the high-voltage retarding grid, grounded grids, and an electron repelling grid biased to −30 V to keep secondary electrons produced by

Table 1 Most common ion clusters present in EMI-BF_4 ion beams.

Polarity	Degree of Solvation	Mass [amu]
Positive (EMI^+ cation)	$n = 0$	111.2
	$n = 1$	309.2
	$n = 2$	507.2
Negative (BF_4^- anion)	$n = 0$	86.8
	$n = 1$	284.8
	$n = 2$	482.8

Table 2 Common fragmentation events in EMI-BF_4 ion beams.

Polarity	Fragmentation Event	Mass Fraction
Positive (EMI^+ cation)	$n = 2 \rightarrow n = 0$	0.22
	$n = 1 \rightarrow n = 0$	0.36
	$n = 2 \rightarrow n = 1$	0.61
Negative (BF_4^- anion)	$n = 2 \rightarrow n = 0$	0.18
	$n = 1 \rightarrow n = 0$	0.30
	$n = 2 \rightarrow n = 1$	0.59

collisions with the upstream grids from interfering with the current signal. RPA measurements also give insight into ion fragmentation processes that occur inside and outside the thruster. Fragmentation occurs when a solvated ion, or an ion attached to a single or cluster of neutral molecules, breaks up into a neutral molecule and a lighter ion. These fragmentation events show up in RPA curves because when an cluster breaks apart, the sum of the energies of the resulting fragments is equal to the total pre-fragmentation energy of the cluster, which is approximately the energy gained during acceleration through the applied electric field (the beam energy).

If a cluster fragments outside of the thruster when it is no longer accelerating (the field-free region), its post-fragmentation energy will be a predictable fraction of the beam energy, depending on the degree of solvation of both the pre- and post-fragmentation ions. The most common species present in the beam are typically isolated ions or monomers (degree of solvation $n = 0$), ions attached to a single neutral particle or dimers ($n = 1$), and ions attached to a cluster of two neutrals or trimers ($n = 2$). Table 1 gives the masses of each cluster type for both positive EMI^+-based ions and negative BF_4^--based ions.

Based on the most plentiful species in the beam (Table 1), the most common fragmentation events are expected to be fragmentation of trimers into monomers, dimers into monomers, and trimers into dimers. Since clusters that fragment outside of the acceleration region have reached their terminal velocity, the energy fraction of the fragmented ion is equal to its mass fraction relative to the original cluster. These mass fractions for EMI-BF_4 are given in Table 2. For field-free region fragmentation events, the mass fractions are equal to the energy fractions.

Clusters that fragment inside the acceleration region have a more complex energy distribution. For a singly-charged parent cluster that breaks into a neutral particle and a singly-charged child cluster, the charged species experiences different acceleration magnitudes before and after the fragmentation event. Therefore, the energy fraction of the fragmented species is not a simple mass fraction. Rather it depends on both the initial and final masses and the location in the acceleration region at which fragmentation occurs. Because fragmentation events are typically distributed spatially throughout the acceleration region, the result is a distribution of ion energies that fall between the energies associated with field-free fragmentation events listed in Table 2.

3. Time of Flight Mass Spectrometry

Time of flight mass spectrometry is used to determine the average charge-to-mass ratio of the beam ions, an indicator of specific impulse. It is achieved by using high-resolution instruments to measure the time for particles in the beam to traverse a known distance. The velocity of a particle accelerated from rest through a potential difference has a one-to-one

relationship with its charge-to-mass ratio. Since the beam is heterogeneous, TOF is used to obtain a spectrum of all charge-to-mass ratios that exist in the beam, and average properties like thrust and specific impulse can be deduced therein by integration.

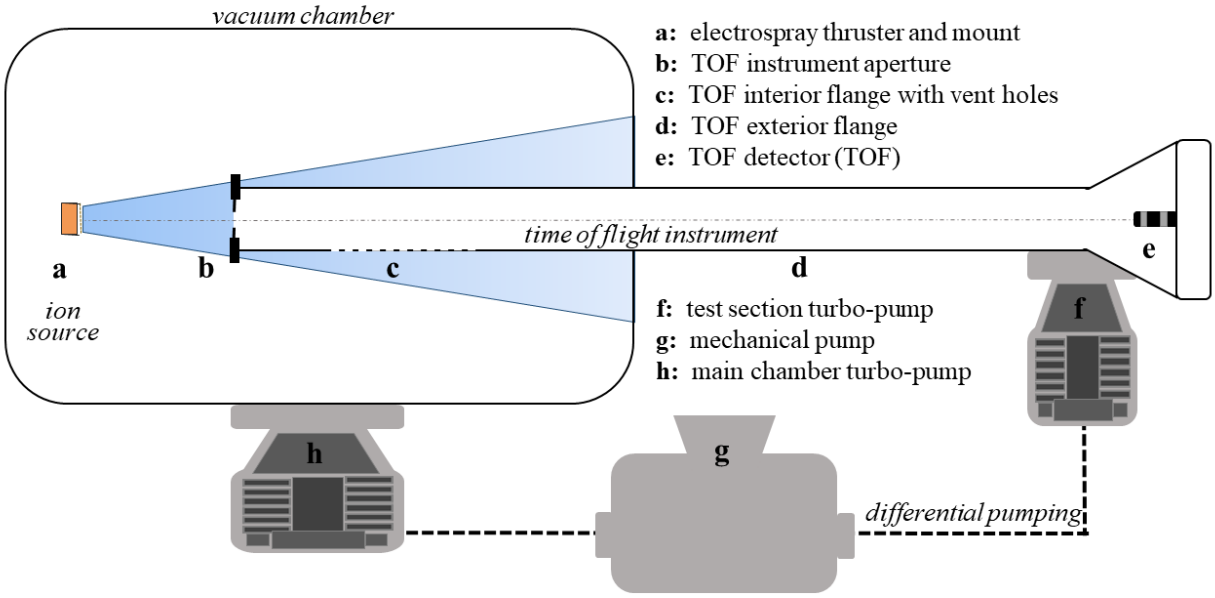

Fig. 4 Diagram of the TOF used in the electrospray tests in the SPL

Fig. 4 shows a diagram of the SPL TOF instrument. The ion beam is directed through an aperture near the ion source where it encounters a deflecting gate biased to ±950 V and controlled by a square waveform to start and stop the beam's path toward the downstream detector in regular intervals. The beam travels through a long isolated tube (length approximately 1 m) before it is its signal is amplified by a Channeltron channel electron multiplier (CEM), which amplifies the signal with a gain of at least 10^7.

TOF measurements are used to calculate properties of the beam by balancing an ion's electric potential energy at emission with its kinetic energy after acceleration,

$$qV_0 = \frac{1}{2}mc^2 \tag{1}$$

Equation 1 relates an ion's expected velocity, c, to its charge-to-mass ratio, q/m. Equation 2 gives the thrust of a rocket engine in vacuum with flow rate $\dot{m}$ and exhaust velocity c. Together, we arrive at a relationship for the total thrust output of an electrospray that emits more than one ionic species, with the i-th species having charge-to-mass ratio $(q/m)_i$ and current contribution I_i. The result is equation 3.

$$F = \dot{m}c \tag{2}$$

$$F = \sum_i I_i \sqrt{\frac{2V_0}{(q/m)_i}} \tag{3}$$

A raw TOF signal gives current as a function of time, t, rather than q/m directly. The velocity of the ion is related to the known length of travel, L, and the measured time of travel by $c = L/t$. So, we can combine equation 3 with equation 1 and $c = L/t$ to write,

$$F = \sum_i I_i \frac{2V_0}{L} t_i \tag{4}$$

Or for a continuous spectrum of species, the summation can be written as an integral,

$$F = \frac{2V_0}{L} \int_0^\infty I(t)dt \tag{5}$$

Equation 5 can be used to indirectly estimate thrust from a TOF measurement. Note we must assume that all species are singly-charged ions. If a significant amount of multiply-charged ions or neutral species exist in the beam, equation 5 becomes decreasingly accurate. A similar derivation leads to an estimate of mass flow rate $\dot{m}$ as a function of $I(t)$,

$$\dot{m} = \frac{4V_0}{L^2} \int_0^\infty I(t)tdt \tag{6}$$

Furthermore, equations 5, 6, and 2 can be used to compute estimates for thrust, mass flow rate, and specific impulse of an electrospray thruster given a TOF signal of the form $I(t)$.

4. Angular Beam Distribution

Beam divergence information is taken by measuring the current density of the thruster plume at different angles relative to the thruster centerline. Beam divergence measurements are a key contributor to estimates of overall thruster efficiency, as only the component of ion velocities normal to the thruster face contribute usefully to trust.

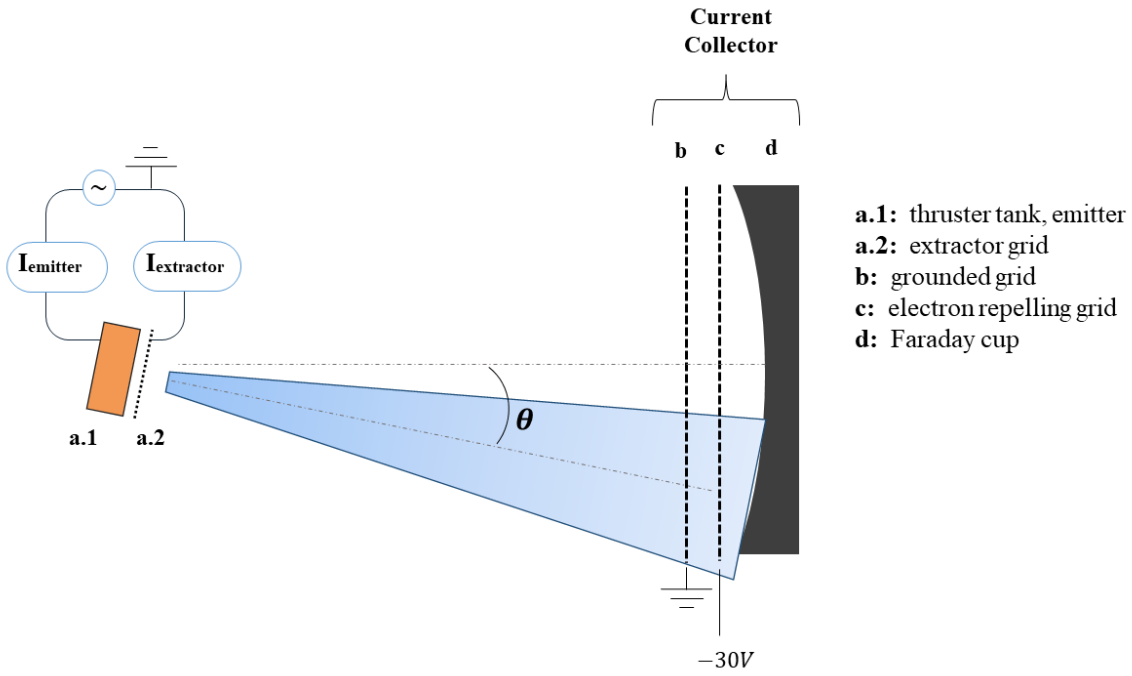

Fig. 5 Diagram of the angular beam distribution measurement setup used in the electrospray tests in the SPL

Beam divergence data is measured by firing the thruster at a Faraday cup current collector and varying the angle θ between the thruster and collector centerlines. The result is a measure of current as a function of θ.

B. Test Results and Performance Metrics

A current-voltage curve was measured by applying a triangular voltage waveform to the emitter electrode with an amplitude of 1300 V and a period of 60 seconds. Current emitted by the emitter and intercepted by the extractor are independently tracked as voltage is swept, generating a relationship between voltage and current. The waveform is repeated three times and the data are averaged. The resulting IV curve is shown in Fig. 6.

Key metrics attainable from the IV curve include startup voltage and transmission efficiency, or the efficiency of the process of extracting ions through the extractor grid. Transmission efficiency is defined as

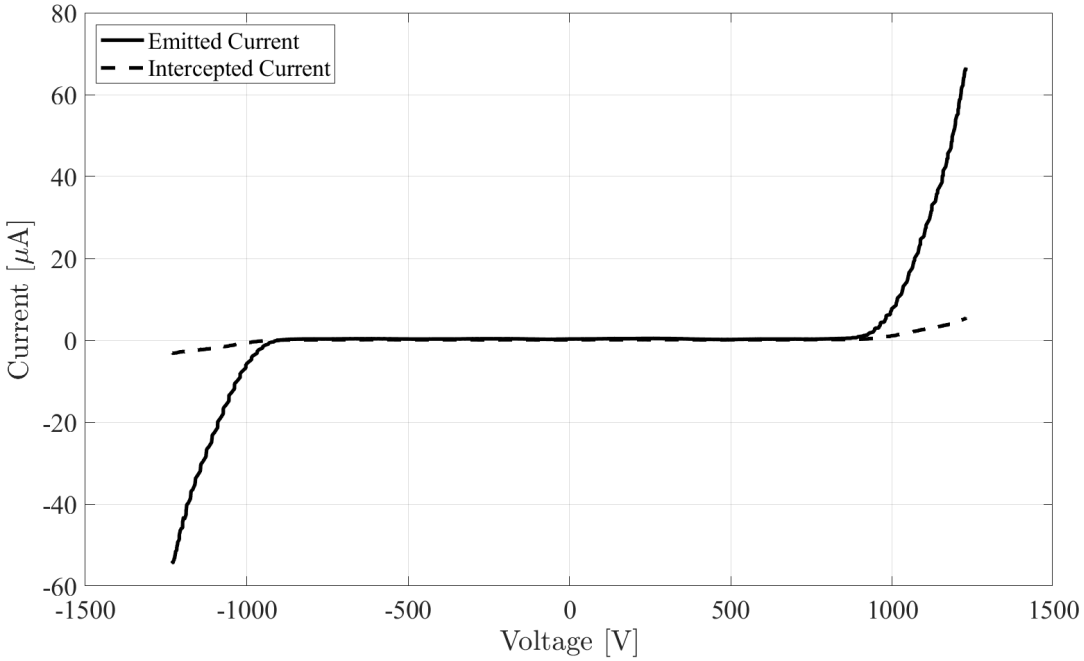

Fig. 6 Current-Voltage characteristic curve of a densified silicon thruster.

$$\eta_{tr} = \frac{I_{em} - I_{int}}{I_{em}} \tag{7}$$

Transmission efficiency can be interpreted as the fraction of emitted current that contributes to thrust, since current intercepted by the extractor does not exert a net force on the thruster. The IV curve in Fig. 6 yielded an average transmission efficiency of $\eta_{tr} = 0.907$.

Retarding potential analysis measurements are taken with the thruster firing in a steady state condition. The RPA measurement for the silicon thruster was taken with the thruster firing at potential V_0 = 1300 V and emitting a steady current of approximately 71 μA. With the thruster firing into the RPA diagrammed in Fig. 3, a triangular voltage waveform is applied to the retarding grip. V_{RPA} is swept between −200 V and +1500 V to encompass all ion energies expected in the beam. Current arriving at the Faraday cup downstream of the retarding grid is collected, yielding a relationship between V_{RPA} and collected current. The resulting RPA curve is shown in Fig. 7.

RPA measurements yield information about fragmentation events occurring both inside and outside of the thruster as well as the efficiency with which electric potential energy is being converted to ion kinetic energy. This efficiency is known as energy efficiency, and it is the ratio of the beam potential to the applied firing potential.

$$\eta_E = \frac{V_B}{V_0} \tag{8}$$

where V_B and V_0 are the beam potential and applied firing potential, respectively. The beam potential can be estimated as the maximum peak in the ion energy spectrum, which is found by taking a derivative of the RPA curve in Fig. 7 with respect to V_{RPA}. Since a derivative of a discrete signal must be performed, the quality of the signal and the amount of noise present can greatly impact the estimate for η_E, and it is therefore difficult to obtain highly accurate η_E measurements. The beam potential was found to be approximately $V_B \approx 1170$ V at an applied potential of V_0 = 1300 V, yielding an energy efficiency of approximately $\eta_E \approx 0.900$.

Time of flight measurements, like RPA measurements, are acquired with the thruster firing at a steady condition. The TOF measurement for the silicon thruster was taken with the thruster firing at approximately the same conditions as it was during the RPA measurement. The beam is directed through an aperture toward the TOF instrument, and the gate is enabled to interrupt the beam at regular intervals. Downstream, the CEM current amplifier collects current as a function of time after each gate opening. A TOF curve of one of the silicon thrusters is shown in Fig. 8.

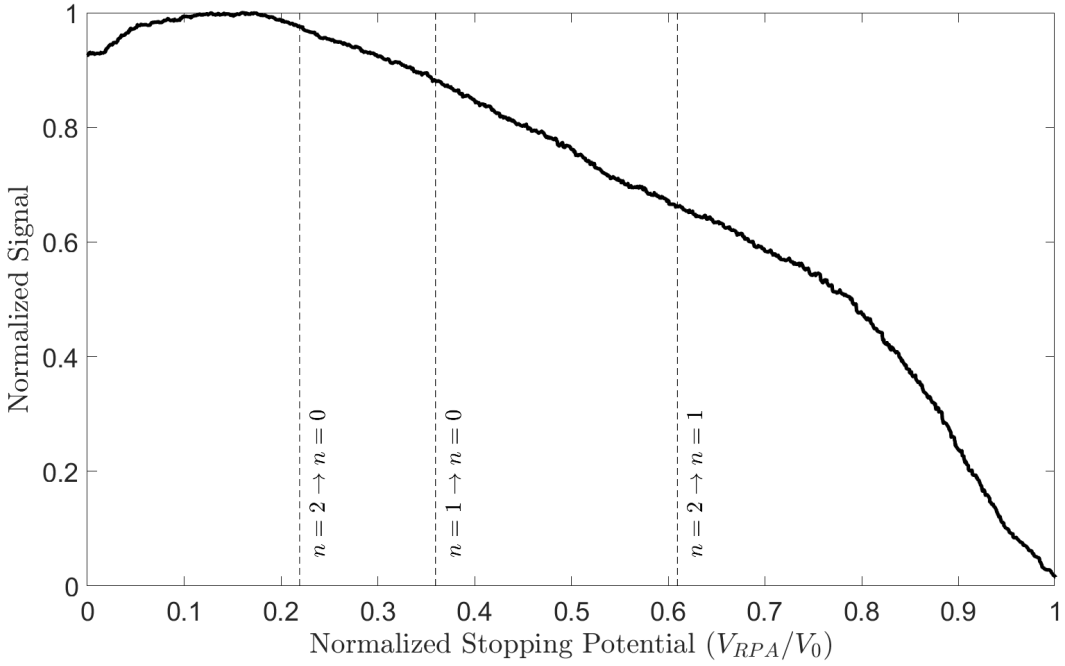

Fig. 7 RPA curve of a densified silicon in the positive polarity.

As discussed in section III.A, several key performance metrics can be estimated from TOF results, including thrust, specific impulse, mass flow rate, and polydispersive efficiency. Polydispersive efficiency is a measure of energy losses due to accelerating ions and clusters of varying specific charge, and it is one of the primary efficiency losses in electrospray thrusters. Polydispersive efficiency can be estimated using TOF data from equation 9 [7].

$$\eta_p = \frac{F_{TOF}^2 / 2\dot{m}_{TOF}}{I_{em} V_0} \tag{9}$$

Polydispersive efficiency is a significant loss in electrosprays because there is frequently a polydisperse composition of ions in the beam, and the energy spent accelerating the faster ones is greater than the extra thrust derived from them. The TOF curve in Fig. 8 yielded a polydispersive efficiency of $\eta_p = 0.506$. Thrust, specific impulse, mass flow rate estimates from the TOF curve are listed in Table 3.

Finally, the beam divergence measurements were taken with the thruster firing at steady state with $V_0 = 1000$ V and $I_{em} = 32$ µA. The thruster is fired at the Faraday cup while mounted on a rotational stage, and the angle between the thruster and collector centerlines is linearly swept between ±45° a total of six times and the collected current as a function of angle θ is recorded and averaged across the six repetitions. The beam divergence data for the silicon thruster is presented in Fig. 9.

From the beam divergence measurement, we are able to ascertain the angular efficiency of the thruster, which is a projection of the beam's momentum along the axis normal to the thruster face compared to the ideal case in which the entire beam was emitted normal to the thruster face. To estimate the angular efficiency, the beam is assumed to be axisymmetric with composition and properties that do not vary with time or angle. With these assumptions, the angular efficiency can be calculated as,

$$\eta_\theta = \left(\frac{\int_0^{\frac{\pi}{2}} I(\theta) \cos\theta \sin\theta d\theta}{\int_0^{\frac{\pi}{2}} I(\theta) \sin\theta d\theta} \right)^2 \tag{10}$$

Prior to computing η_θ using equation 10, the beam divergence data was smoothed and centered around a central firing angle. The central angle θ_c was computed by solving equation 11.

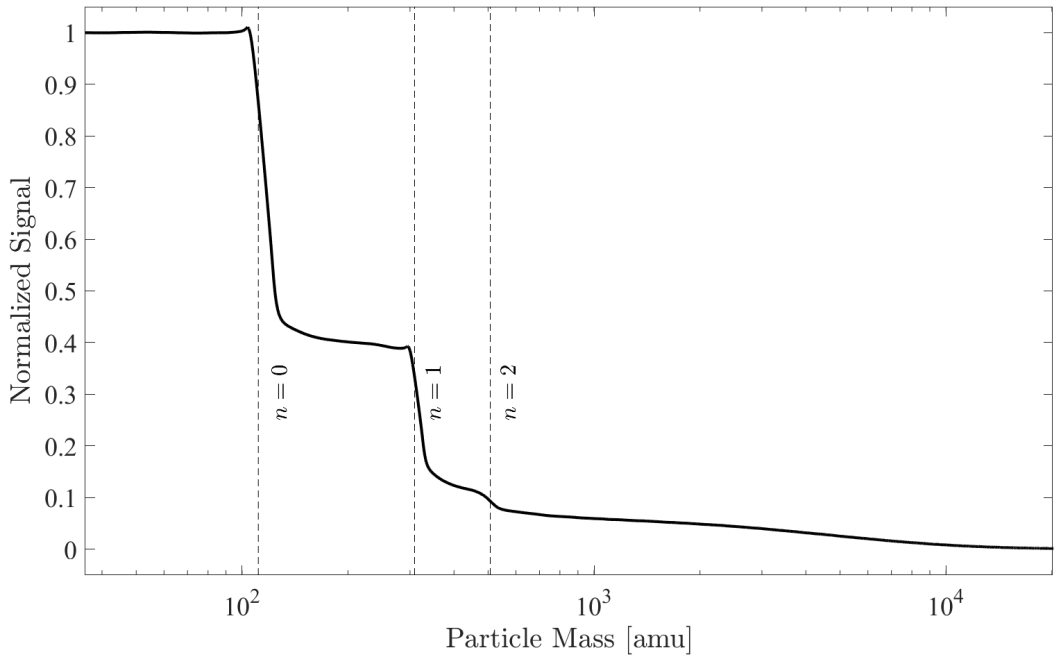

Fig. 8 TOF curve of a densified silicon in the positive polarity.

Table 3 Performance metrics of densified silicon thrusters from diagnostic data. Data is for positive mode only.

Performance Metric	Estimate
F	6.3 µN
$\dot{m}$	0.43 µg/s
I_{sp}	1499 s

$$\int_{-\frac{\pi}{2}}^{\theta_c} I(\theta)d\theta = \int_{\theta_c}^{\frac{\pi}{2}} I(\theta)d\theta \tag{11}$$

The angular efficiency for the silicon thruster at this operating point was estimated to be $\eta_{\theta+} = 0.919$ $\eta_{\theta-} = 0.909$ for the positive and negative modes, respectively.

The total thruster efficiency, η_T, is the percentage of supplied electrical power that is converted to usable beam power, and it can be estimated using equation 12, as in [8] and [3].

$$\eta_T = \frac{P_T}{P_E} = \frac{\frac{1}{2}F^2/\dot{m}}{IV_0} = \eta_i \eta_{tr}^2 \eta_\theta \eta_E \eta_p \tag{12}$$

The ionization efficiency η_i is typically taken as unity for electrospray thrusters, which amounts to an assumption that no neutral species evaporate from the ionic liquid. Taking the individual efficiencies calculated above, the total thruster efficiency can be estimated to be $\eta_T = 0.344$. The total efficiency for the tested thrusters is low compared to published efficiencies for EMI-BF_4 electrosprays in the pure ion regime, estimates for which range from about 60% [3] as high as 90% [8]. However, the densified silicon thruster is in a prototypical state and far from optimized. Future work will iterate on the design of the densified thrusters to achieve better fabrication precision, tailored fluid control, and improved and more repeatable assembly/alignment processes. These future iterations will be expected to improve in areas that contribute most detrimentally to efficiency, such as transmission and polydispersion. Table 4 gives a complete list of the efficiencies for the densified silicon thruster in the positive mode.

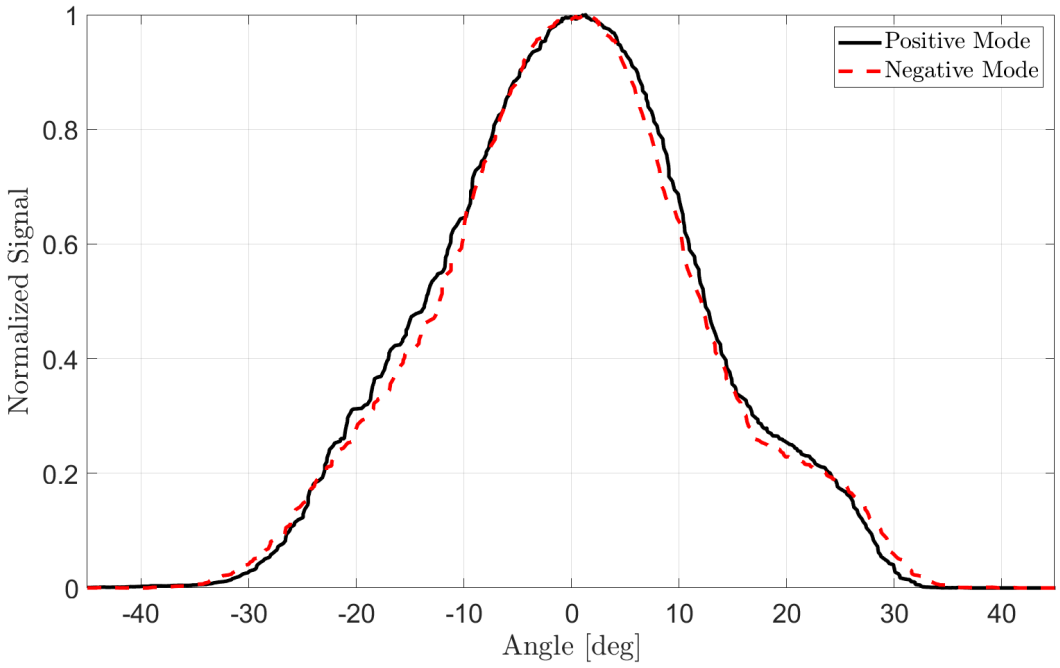

Fig. 9 Angular beam distribution of a densified silicon thruster in both the positive and negative polarities.

Table 4 Efficiency estimates of densified silicon thrusters from diagnostic data. Data is for positive mode only.

Efficiency	Estimate
η_{tr}	0.907
η_E	0.900
η_p	0.506
η_θ	0.919
η_T	0.344

IV. Direct Thrust Measurement

Measurement of thrust is one of the most critical yet difficult aspects of characterizing thrusters for space propulsion, as demand for smallsat-scale propulsion systems has necessitated the development of thrust stands capable of measuring force at the μN level, which requires extremely sensitive and carefully designed instruments. In laboratory settings, thrust from electric propulsion devices is typically measured using pendulum-based thrust stands [9], which measure force by tracking the motion of a pendulum in response to forces or torques delivered by a thruster. Several groups have developed and used pendulum-based thrust stands to directly measure thrust of electrospray, colloid, and FEEP thrusters. In the early 2000s Busek [10] and NASA JPL [11] built torsional thrust stands capable of resolving thrust below the μN level. Later versions of these same thrust stands were used by Busek in 2008 during the development of the Colloid Micro Newton Thruster (CMNT) that flew on the LISA Pathfinder mission [12] and by Legge and Lozano in 2011 to characterize one of the first generations of ionic liquid electrospray thrusters based on porous emitter arrays [13].

Pendulum thrust stands carry many disadvantages. Noise is introduced as a result of the thrust stand being fixed to its environment, and extremely small displacements need to resolved with great accuracy. The latter issue is often mitigated by the use of null-type thrust stands, which through closed-loop control apply an equal and opposite force on the thruster to keep it fixed in place. While systems that keep the thruster motionless help to alleviate errors to to movement of the thruster, environment noise remains a factor and additional uncertainty is introduced in the restoration force and control system.

Courtney in 2016 used a sensitive mass balance to directly measure thrust of an ionic liquid electrospray system, and the results were compared to indirect thrust measurements calculated from time of flight mass spectrometry [14]. Alternative instruments have been developed to isolate the thrust stand from its environment to decrease the influence of random errors on thrust measurements. One such instrument is a magnetically-levitating thrust balance where a test vehicle is magnetically levitated in order to provide one friction-less rotational degree of freedom [15]. Thrusters can then be used to produce torques on the test vehicle, and by measuring the resulting change in rotation of the test vehicle the thrust can be inferred [16]. The densified silicon electrospray thrusters were tested on the magnetically levitated thrust stand to verify their performance.

A. Magnetically Levitated Thrust Stand

The magnetically levitated thrust stand (MagLev) in the SPL was designed by Fernando Mier-Hicks and SPL personnel in the 2010s. Its advantages of being contact-free and having 360 degrees of rotational freedom around one axis permit direct thrust measurements with extremely high measurement resolution and allow for more complex thruster tests in addition to direct thrust measurements, including precise angular control experiments [17].

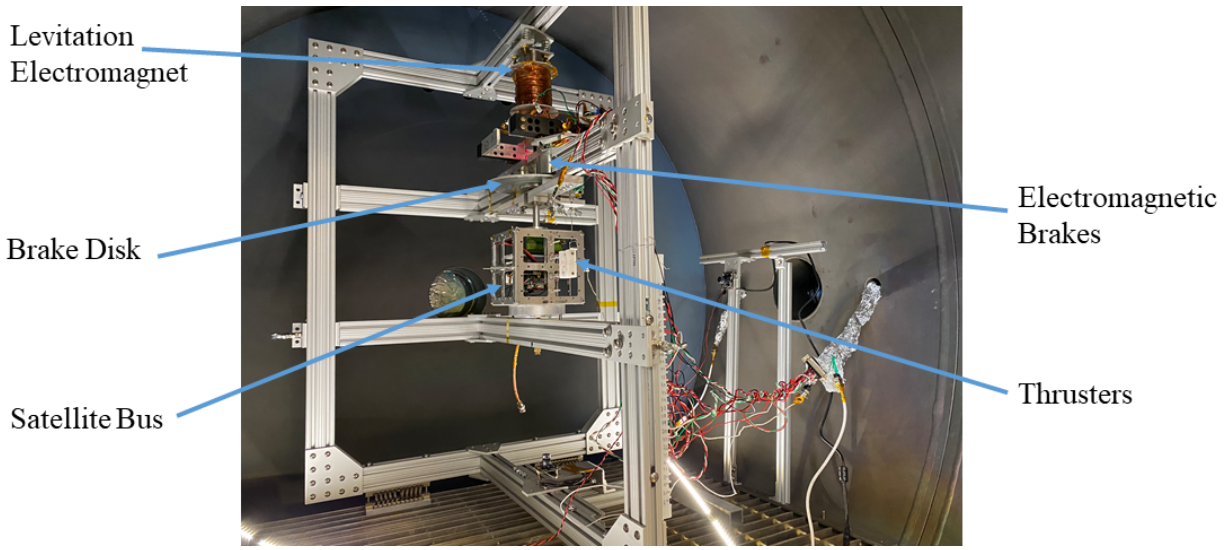

Fig. 10 Image of the MagLev thrust stand inside the AstroVac vacuum chamber in the SPL.

An image of MagLev with some of the critical components highlighted is shown in Fig. 10. The thrust stand is comprised of an external structure that is fixed inside a vacuum chamber and a levitated structure that is suspended using magnetic forces within the fixed structure. The fixed structure contains the majority of the electronics, and contact-free actuators and sensors required for MagLev to operate. It also houses the command and telemetry streams that are routed through the chamber wall to a computer for remote operation. The primary component of the levitated structure is a 13 cm cubic satellite structure with a dedicated power system, on-board computer, and propulsion power processing unit (PPU). The test thrusters are mounted to the satellite structure such that they produce torque about the satellite center vertical axis. Attached to the satellite and therefore part of the levitated structure are several components such as conducting disks, permanent magnets, and optical sensor flags that allow the levitated structure to interact with the fixed structure with making physical contact.

Stable levitation is achieved by interaction of a permanent magnet on the levitated structure and an electromagnet on the fixed structure. An optical sensor detects the vertical position of the satellite relative to its stable levitation point, and a PID controller uses the vertical position sensor feedback to control the current through the electromagnet to hold the satellite position steady within 10 μm of the levitation setpoint. The fixed structure houses two additional electromagnets which, when activate, generate eddy currents in a conducting disk on the levitated structure when it is in motion, which acts as an electromagnetic brake.

MagLev's on-board PPU is capable of controlling up to four thrusters at once. It is comprised of a printed circuit board (PCB) that houses microcontrollers, power electronics, and sensor circuits necessary to operate electrospray thrusters. Adjustable high-voltage amplifiers can generate emitter potentials up to 1500 V. While electromechanical

relays on the PPU allow the operator to switch between several different electrical configuration, the nominal operation mode involves operating thrusters in pairs, with the two thrusters in each pair emitting current of equal magnitude but opposite polarity. This mode of operation maintains electrical neutrality of the satellite bus, which is a critical consideration for MagLev since the satellite is electrically isolated from the external facilities during operation. If the net current out of the satellite deviates from zero, the satellite bus will charge at a rate dependent on the satellite's self capacitance. If the satellite is allowed to charge to large potentials, emitted ions can be attracted back to the satellite, negating the thrust and potentially damaging satellite components and electronics. The thruster pair's currents are constrained to be equal and opposite by connecting their emitters in series and galvanically isolating the high-voltage thruster circuit from the low-voltage PPU electronics. Such a configuration ensures that the magnitude of current that flows through both thrusters is equal.

The most critical measurement during a direct thrust measurement on MagLev is the satellite's angular position because the thrust produced is inferred directly from the response of the satellite's angular position. Angular position is measured using a webcam-based optical sensor mounted underneath the levitated structure. Without making physical, the webcam views a fiducial pattern printed on the bottom face of the satellite, and software is used to interpret the pattern and calculate the angular position relative to an arbitrary zero.

B. Measurement Principles

A thrust measurement is taken on MagLev by starting with the satellite at rest or in a small oscillation. The satellite oscillates when levitating due to imperfections in the structure of the magnetic field inside the vacuum chamber that interact with the permanent magnet on the levitated structure in a way that causes undamped oscillation. The MagLev fixed structure is equipped with two pairs of Helmholtz coils to negate the effects of the magnetic disturbance and minimize the frequency of the oscillations, but some level of oscillation typically persists. More details regarding the nature and mitigation of these oscillations can be found in [18].

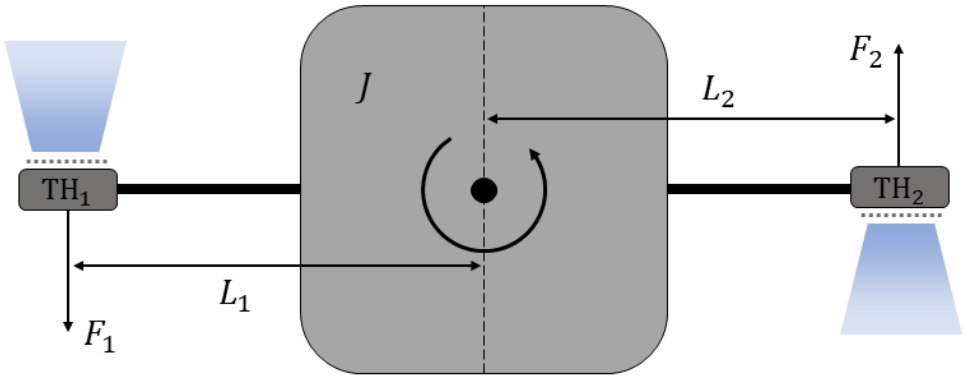

Fig. 11 Top-down diagrammatic view of the MagLev satellite with thrusters firing to impart a torque around the central axis and rotate the satellite counterclockwise.

With the satellite at an approximate rest, the thrusters are turned on in unison and with equal but opposite current. The expected response is an angular acceleration, α, of the satellite dependent on thrust, F, moment of inertia, J, and moment arm of the thruster torque, L. The moment arms and moment of inertia are measured prior to testing. An illustration of each of these parameters on the MagLev satellite is shown in Fig. 11. The equation of motion can be written as,

$$J\alpha = F_1 L_1 + F_2 L_2 \tag{13}$$

Since L_1 and L_2 are design parameters, they can be made equal so that equation 13 simplifies to

$$F_{tot} = \frac{J\alpha}{L} \tag{14}$$

where F_{tot} is the combined force of the two thrusters, $F_{tot} = F_1 + F_2$, and $L = L_1 = L_2$. Angular acceleration is determined from the measured angular position. Average angular acceleration and therefore average thrust can be

determined over a long firing period, or for sufficiently smooth data instantaneous thrust can be determined at each point in time.

C. Experimental Results

A pair of 729-tip, 127-µm-pitch thrusters was used for the direct thruster measurement. Each thruster was supplied with 10 µL of EMI-BF_4 via wicks placed on the back of the emitters, and a porous carbon distal electrode made electrical contact between the propellant and the high voltage supply on the PPU. Prior to the experiment, the vacuum chamber was pumped to $< 5 \times 10^{-5}$ Torr using the combined pumping capacity of Edwards Brooks OB-400 and CT-10 cryopumps. During pumpdown, the satellite is levitated so that any undesired motion remaining from the initiation of levitation is slowly dampened over time, resulting in a satellite experiencing pure rotation about its central axis at the start of the test.

Immediately prior to firing the thrusters, the Helmholtz coils are calibrated to minimize the frequency and amplitude of oscillations. When the oscillations are minimized and the satellite has reached a stable state, the thrusters are commanded to fire at a prescribed voltage. Though the voltage is the parameter that is controlled, the constraint on the thruster circuit discussed in section IV.A will cause the emitted currents to equalize (but in opposite polarities) while the actual potential difference across the thruster electrodes adjusts itself to satisfy the constraint. In this way, if the two thrusters are not identical in their emission characteristics, one of them will limit the pair. For example, if it is desired to maximize thrust by applying the maximum voltage allowable on the PPU, the weaker thruster will emit some amount of current at that maximum voltage while the stronger thruster emits the same current but at a lower voltage.

During the experiment, the thrusters were fired continuously for 30 minutes, increasing the angular velocity of the satellite from 0 to approximately 3.5°/s. The shape of the angular velocity profile suggests that the acceleration experienced by the satellite can be attributed directly to the torque induced by the thrusters.

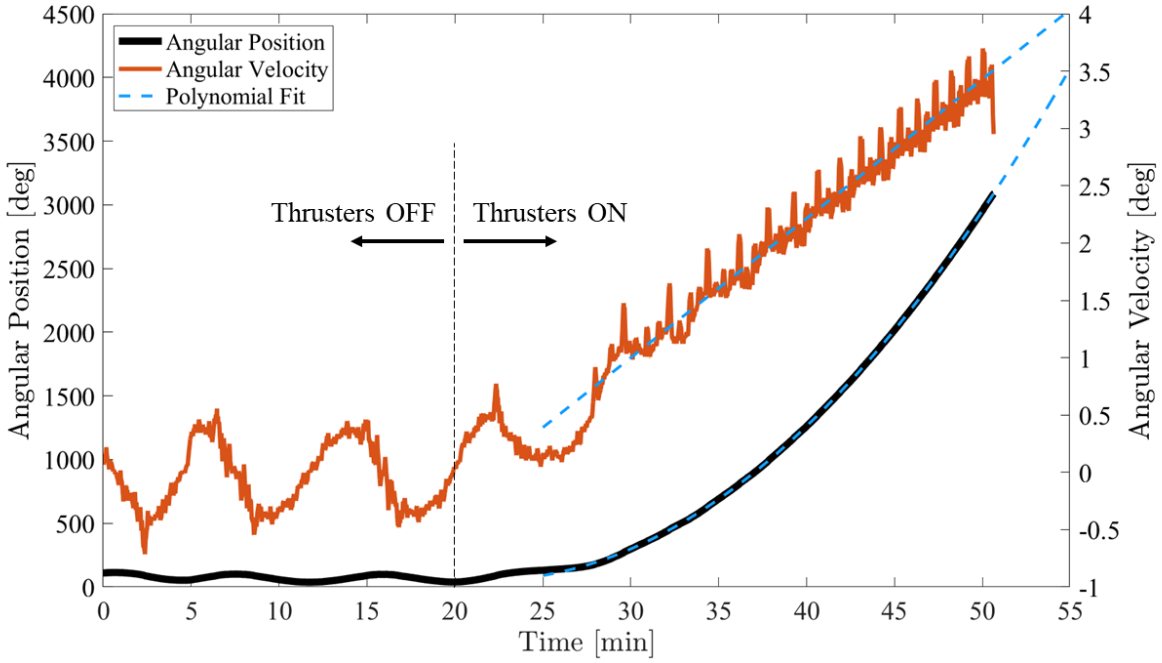

Fig. 12 Angular position and velocity data acquired during the direct thrust measurement test of the densified silicon thrusters.

Fig. 12 shows the the measured angular position data, which was numerically differentiated to produce the angular velocity profile. A quadratic polynomial was fit to the position data, and the derivative of the quadratic model was used to approximate the angular velocity. The polynomial fits agreed very well with the measured data. The slope linear angular velocity model was used to calculate α, which was found to be $\alpha = 0.035$ mrad/s^2. The moment of inertia was measured prior to the test using a trifilar pendulum, and the moment arm was measured using a ruler, resulting in $J = 0.00557$ kg m^2 and $L = 13.1$ cm. Using equation 14, the total thrust was calculated to be $F = 1.5$ µN. Throughout

the test interval, the thrusters were operating at an emission current of approximately 3.4 μA per thruster. It is not possible to differentiate the thrust contributions from the individual thrusters without additional information and data points. Since it is known that both thrusters emit equal current magnitudes, it can be safely assumed that the two thrusts will be comparable. However, differences in the firing voltage and the beam composition of the two thrusters nearly eliminates the possibility of the two thrusts being equal. Under the approximation that the two thrusts are similar, each thruster contributed about 0.75 μN, which is in good agreement with the expected thrust at 3.4 μA of current estimated from TOF measurements.

Since it is necessary to fire two thrusters simultaneously on the MagLev thrust stand so that pure torque is produced and spacecraft neutrality is maintained, future work will address the problem of properly differentiating the two thrust contributions, which is possible to do with a carefully selected pair of thrusters and sufficient information about their characteristics. A methodology for separating the thrust contributions is proposed and tested in [19].

V. Conclusion

Here, a preliminary framework is proposed for future improvements to the performance characteristics of ionic liquid electrospray propulsion systems, with thrust density as the driving figure of merit. One methodology by which thrust density can be augmented is decreasing emitter pitch to increase the packing density of emitting tips. Increasing emitter packing density necessitates the use of different materials and more advanced fabrication techniques to create highly complex three-dimensional geometries at the microscopic scale, but it leverages well-understood principles of electrospray physics and is therefore relatively predictable and reliable.

Increasing the thrust density of electrospray thrusters requires increasing the current emitted per unit area, the effects of which are not yet widely understood. Several factors that are typically considered negligible in electrosprays, such as heat dissipation and space charge, may become significant at increased current densities, and the critical point at which phenomena such as these must be considered is not yet known. For this work to be continued, it is likely necessary to take an in-depth look at the physics of ion emission in electrospray thrusters at the molecular level to better understand the factors that will significantly influence macroscopic thruster performance. The tests performed here serve merely as proofs of concept for the principles and ideas that may lead not only to a better understanding of electrospray thrusters but also improved designs that can potentially have an enormous impact on the market for small spacecraft propulsion.

Emitter arrays fabricated using grayscale lithography from silicon with pitch as low as 127 μm were tested for the first time as an integrated thruster system with an extractor grid electrode and ionic liquid propellant. Initial performance of the densified arrays was promising, with evidence of repeatable and stable emission in the pure ionic regime and current levels consistently exceeding 70 μA at voltages on the order of 1 kV.

Several performance characteristics of the densified silicon thrusters were measured both directly and indirectly using test equipment and diagnostics in the Space Propulsion Laboratory at MIT. Current-voltage measurements, retarding potential analysis, time of flight mass spectrometry, and beam divergence measurements were performed and compiled to obtain an overall view of the preliminary performance and efficiency of the thrusters. Finally, a magnetically levitated thrust stand was used to measure thrust directly.

A. Future Work

Work to further develop the proof of concept covered here is necessary to push forward the state of the art in electrospray propulsion. The propulsion systems tested here are prototypes, and therefore further iteration and development of their designs will yield clearer experimental results.

For instance, it has been proven that the densified MEMS emitters can emit a pure ion beam and produce measurable thrust, as observed via diagnostic data and demonstrated using a magnetically levitated thrust stand. However, the novel thruster concept is still in development, and its performance characteristics are expected to change as design details, including those having to do with emitter-extractor interfaces and fluid control, are matured.

An immediate next step in the development of the densified thrusters is to acquire long-duration firing data, which was not able to be obtained up to this point. Long duration data yields information regarding the evolution of the thruster's behavior over time and the maximum achievable lifetime. It also enables direct measurements of the average mass flow rate over a firing duration, since propellant mass consumption approaches levels that can be measured using laboratory scales. Firing for long durations (hundreds of hours) requires a propellant tank to store the volume of ionic liquid needed for such a test. The design for the iEPS ionic liquid propellant tank developed by MIT [4, 20, 21] has been extensively tested and qualified for space flight, so development of an interface between the silicon thrusters and the iEPS tank is underway. The long term outlook for the silicon thrusters may involve development of a new tank design

tailored toward the needs of classes of satellites even smaller than the cubesats for which the iEPS was designed.

Additionally, the characterization of the 127-µm-pitch thrusters has successfully provided a foundation for continued development of an ultra-dense 64-µm-pitch version of the silicon thrusters. Decreasing pitch to these levels has the potential to increase thrust density by a factor of 60 compared to the state of the art, possibly making electrospray propulsion technology competitive with traditional electric propulsion in terms of areal thrust density. Silicon emitter arrays with pitch as low as 64 µm have been tested without extractor grids in previous works, and the results presented here are a significant step toward the eventual testing and deployment of these ultra-dense devices as integrated thrusters.

Ultimately, since the densified silicon thrusters have been demonstrated in the laboratory, it will be beneficial to conduct an on-orbit demonstration of the technology to further develop and qualify the technology. On-orbit demonstrations provide the most reliable data for a thruster's ability to survive the harsh conditions of launch and perform in space. Since a satellite's position can be tracked very accurately, information about the propulsion system's performance can be inferred via measurement of changes in orbital elements in response to a known thruster command. Similar demonstrations for new propulsion systems are performed frequently, and they are the only way for a technology to graduate to a technology readiness level (TRL) of 9.

Acknowledgments

DISTRIBUTION STATEMENT A. Approved for public release. Distribution is unlimited. This material is based upon work supported by the Under Secretary of Defense for Research and Engineering under Air Force Contract No. FA8702-15-D-0001 and by the National Science Foundation Graduate Research Fellowship under Grant No. 1745302. Any opinions, findings, conclusions or recommendations expressed in this material are those of the author(s) and do not necessarily reflect the views of the Under Secretary of Defense for Research and Engineering.

References

[1] Cidoncha, X. G., Kristinsson, B. Ö., and Lozano, P. C., "Informing the Design of Pure-ion Electrospray Thrusters via Simulation of the Leaky-Dielectric Model with Charge Evaporation," *36th International Electric Propulsion Conference*, Vienna, Austria, 2019, pp. IEPC–2019–610.

[2] Coffman, C. S., Martínez-Sánchez, M., and Lozano, P. C., "Electrohydrodynamics of an ionic liquid meniscus during evaporation of ions in a regime of high electric field," *Phys. Rev. E*, Vol. 99, No. 6, 2019, p. 063108. https://doi.org/10.1103/PhysRevE.99.063108.

[3] Petro, E. M., Bruno, A. R., Lozano, P. C., Perna, L. E., and Freeman, D. S., "Characterization of the TILE Electrospray Emitters," *AIAA Propulsion and Energy 2020 Forum*, 2020, pp. AIAA–2020–3612. https://doi.org/10.2514/6.2020-3612.

[4] Kristinsson, B. Ö., Freeman, D., Petro, E., Lozano, P. C., Hsu, A., Young, J. A., and Martel, F., "Operation and Performance of a Fully-Integrated ionic-Electrospray Propulsion System," *36th International Electric Propulsion Conference*, Vienna, Austria, 2019, pp. IEPC–2019–646.

[5] Siegel, N. W., "Silicon Wafer Integration of Ion Electrospray Thrusters," Master's thesis, Massachusetts Institute of Technology, Cambridge, MA, May 2020.

[6] Smith, M. A., Berry, S., Parameswaran, L., Holtsberg, C., Siegel, N., Lockwood, R., Chrisp, M. P., Freeman, D., and Rothschild, M., "Design, simulation, and fabrication of three-dimensional microsystem components using grayscale photolithography," *Journal of Micro/Nanolithography, MEMS, and MOEMS*, Vol. 18, No. 4, 2019, pp. 1 – 14. https://doi.org/10.1117/1.JMM.18.4.043507.

[7] Miller, C. E., "Characterization of ion Cluster fragmentation in ionic liquid ion sources," PhD dissertation, Massachusetts Institute of Technology, Jun. 2019.

[8] Lozano, P., and Martinez-Sanchez, M., "Efficiency Estimation of EMI-BF4 Ionic Liquid Electrospray Thrusters," *41st AIAA/ASME/SAE/ASEE Joint Propulsion Conference & Exhibit*, 2005, pp. AIAA–2005–4388. https://doi.org/10.2514/6.2005-4388.

[9] Polk, J. E., Pancotti, A., Haag, T., King, S., Walker, M., Blakely, J., and Ziemer, J., "Recommended Practices in Thrust Measurements," *33rd International Electric Propulsion Conference*, Washington DC, USA, 2013, pp. IEPC–2013–440.

[10] Gamero-Castaño, M., Hruby, V., and Martínez-Sánchez, M., "A Torsional Balance that Resolves Sub-micro-Newton Forces," *27th International Electric Propulsion Conference*, Pasadena, USA, 2001, pp. IEPC–01–235.

[11] Ziemer, J. K., "Performance Measurements Using a Sub-Micronewton Resolution Thrust Stand," *27th International Electric Propulsion Conference*, Pasadena, USA, 2001, pp. IEPC–01–238.

[12] Hruby, V., Spence, D., Demmons, N., Roy, T., Ehrbar, E., Zwahlen, J., Martin, R., Ziemer, J., Connolly, W., Rhodes, S., and Tolman, W., "ST7-DRS Colloid Thruster System Development and Performance Summary," *44th AIAA/ASME/SAE/ASEE Joint Propulsion Conference & Exhibit*, 2008, pp. AIAA–2008–4824. https://doi.org/10.2514/6.2008-4824.

[13] Legge, R. S., and Lozano, P. C., "Electrospray Propulsion Based on Emitters Microfabricated in Porous Metals," *Journal of Propulsion and Power*, Vol. 27, No. 2, 2011, pp. 485–495. https://doi.org/10.2514/1.50037.

[14] Courtney, D. G., Dandavino, S., and Shea, H., "Comparing Direct and Indirect Thrust Measurements from Passively Fed Ionic Electrospray Thrusters," *Journal of Propulsion and Power*, Vol. 32, No. 2, 2016, pp. 392–407. https://doi.org/10.2514/1.B35836.

[15] Mier-Hicks, F., Perna, L., Coffman, C., and Lozano, P. C., "Characterization of a CubeSat-Compatible Magnetically-Levitated Thrust Balance for Electrospray Propulsion Systems," *49th AIAA/ASME/SAE/ASEE Joint Propulsion Conference*, San Jose, USA, 2013, pp. AIAA–2013–3879. https://doi.org/10.2514/6.2013-3879.

[16] Mier-Hicks, F., and Lozano, P. C., "Thrust Measurements of Ion Electrospray Thrusters using a CubeSat Compatible Magnetically Levitated Thrust Balance," *34th International Electric Propulsion Conference*, Hyogo-Kobe, Japan, 2015, pp. IEPC–2015–148.

[17] Mier-Hicks, F., and Lozano, P. C., "Electrospray Thrusters as Precise Attitude Control Actuators for Small Satellites," *Journal of Guidance, Control, and Dynamics*, Vol. 40, No. 3, 2017, pp. 642–649. https://doi.org/10.2514/1.G000736.

[18] Mier-Hicks, F., "Spacecraft Charging and Attitude Control Characterization of Electrospray Thrusters on a Magnetically Levitated Testbed," PhD dissertation, Massachusetts Institute of Technology, Feb. 2017.

[19] Jia-Richards, O., Corrado, M. N., and Lozano, P. C., "Thrust Inference for Ionic-Liquid Electrospray Thrusters on a Magnetically-Levitating Thrust Balance," *37th International Electric Propulsion Conference*, Cambridge, USA, 2022, pp. IEPC–2022–208.

[20] Krejci, D., and Lozano, P., "Scalable Ionic Liquid Electrospray Thrusters for Nanosatellites," *39th Annual AAS GNC Conference*, Breckenridge, USA, 2016, pp. AAS–16–124.

[21] Krejci, D., Mier-Hicks, F., Thomas, R., Haag, T., and Lozano, P., "Emission Characteristics of Passively Fed Electrospray Microthrusters with Propellant Reservoirs," *Journal of Spacecraft and Rockets*, Vol. 54, No. 2, 2017, pp. 447–458. https://doi.org/10.2514/1.A33531.